Microfluid Nanofluid (2016) 20:20
DOI 10.1007/s10404-015-1671-4

RESEARCH PAPER

Flow regime mapping of high inertial gas–liquid droplet microflows in flow-focusing geometries

Arjang Shahriari[1] · Myeongsub Mike Kim[2] · Siavash Zamani[1] · Nirmala Phillip[1] · Babak Nasouri[3] · Carlos H. Hidrovo[4]

Received: 23 March 2015 / Accepted: 20 October 2015 / Published online: 7 January 2016

Abstract Confined gas–liquid droplet microflows present a lot of new perspectives for microfluidic systems that require the presence of a gaseous phase. In addition to the benefits associated with the discretization of reactive and sensing processes, the highly inertial droplets generated in these systems can enable fast efficient mixing by pair collisions as well as high system throughput due to the short convective timescales involved in the droplet transport. Presented herein is mapping of the geometry-specific droplet generation from a binary gas–liquid flow for different flow-focusing configurations. The dynamic interactions of inertia, shear stress, viscous and surface tension forces create three unique regimes in the gas–liquid flow rate space, providing adaptable flow configuration to specific applications. Analytical investigation and numerical analyses involving governing forces are also introduced to predict the effective droplet diameter versus gas flow rate. We found that the experimental results were well matched to the analytical predictions within 10 % of uncertainty.

Keywords Microfluidics · Droplet generation · High inertia · Flow regime · Flow-focusing geometry

1 Introduction

Droplet-based microfluidics have become ubiquitous and of great importance for applications in biological and chemical fields, including drug delivery (Atencia and Beebe 2004; Yang et al. 2015; Aryafar and Kavehpour 2006; Xu et al. 2009; Marine et al. 2009; Seemann et al. 2012; Li et al. 2008). This is due in part to the discrete nature, precision and programmable controllability that droplets provide (Fair 2007; Link et al. 2006). Droplet flows allow systematic delivery of chemicals or reagents at the nanoliter scale (Sun et al. 2013; Song et al. 2006).

Over the past few decades, existing studies in droplet microfluidics have focused on oil–water systems at very low Reynolds (*Re*) numbers (Bolognesi et al. 2015; van Dijke et al. 2010; Hu and Ohta 2011; Tan et al. 2006; Utada et al. 2005; Yobas et al. 2006). The formation and breakup of droplets in these low *Re* oil–water systems have been explored for various injection geometries including T-junction (Xu et al. 2008; Bedram and Moosavi 2011; Priest et al. 2006; Thorsen et al. 2001) and flow focusing (Roberts et al. 2012; Mulligan and Rothstein 2012; Anna et al. 2003; Zhou et al. 2006). Furthermore, precise controllability of the oil–water droplet flows due to their laminar nature has seen these systems adopted on a wide range of applications such as droplet emulsions (Lorenceau et al. 2005; Hayward

Arjang Shahriari and Myeongsub Mike Kim have contributed equally to this work.

Electronic supplementary material The online version of this article (doi:10.1007/s10404-015-1671-4) contains supplementary material, which is available to authorized users.

✉ Carlos H. Hidrovo
hidrovo@neu.edu

[1] Mechanical Engineering Department, The University of Texas at Austin, 204 E. Dean Keeton Street, Austin, TX 78712, USA

[2] Ocean and Mechanical Engineering, Florida Atlantic University, 777 Glades Road, Boca Raton, FL 33431, USA

[3] Mechanical Engineering Department, The University of British Colombia, 2054-6250 Applied Science Lane, Vancouver, BC V6T 1Z4, Canada

[4] Multiscale Thermal Fluids Laboratory, Mechanical and Industrial Engineering Department, Northeastern University, 360 Huntington Ave., Boston, MA 02114, USA

et al. 2006), droplet fusion (Liu et al. 2007; Chen et al. 2012) and droplet sorting (Tan et al. 2008a, b; Choi and Park 2005; Jung et al. 2013). While extensive analysis of oil–water droplet flows has assisted in developing a broad understanding of digital microfluidics for wet biochemistry applications, they are not suitable for chemical processes that require the introduction of a gas phase such as oxidation, hydrogenation, carbonylation and chlorination (Wada et al. 2006; Gong et al. 2012). Other gaseous-based applications include the detection of airborne particles (Piorek et al. 2007), purification of organic substances (Wheeler et al. 2005), aerosol drug delivery (Dolovich and Dhand 2011), point-of-care diagnostics (Ahn et al. 2004) and simulating a lung pathway (Song et al. 2011). Furthermore, the low *Re* nature of these flows limits the throughput of fluid transport and efficient mixing through droplet collisions in these systems.

Unlike liquid–liquid systems, gas–liquid schemes make it possible to create digital droplet microfluidics systems in applications that require the presence or involvement of a gaseous phase. One research area in gas–liquid systems that has attracted a great deal of attention is formation of monodisperse gas bubbles in liquid flow (Garstecki et al. 2004). Garstecki et al. demonstrated a method which allows simultaneous and independent control of the size of the individual bubbles and volume fraction of the dispersed phase. Another recent study applies an ultrasonic transducer for acoustofluidic control of bubble size in microfluidic flow-focusing configuration (Chong et al. 2015). Generation of CO_2 bubbles and hydrodynamics of the two-phase flow were demonstrated in another study (Buie and Santiago 2009). Also encapsulation of individual gas bubbles in aqueous droplets with high gas volume fractions has been studied (Wan and Stone 2012).

Similarly, liquid droplets in a gaseous environment have been another area of interest in gas–liquid systems (Carroll and Hidrovo 2013; Carroll and Hidrovo 2012a; b; Gopinath and Koch 2001; Bach et al. 2004; Ben-Tzvi and Rone 2010). Currently, most of these applications rely on the use of electrowetting on dielectric (EWOD) for droplet transport and control (Shabani and Cho 2013; Yasuda et al. 2009). However, these are complicated and cumbersome systems that normally require involved multistep fabrication processes and have limited operation range. In contrast, pneumatic-based liquid droplet systems are simpler to implement and can provide more flexibility in terms of droplet generation and range of operation. These systems are also characterized by high *Re* due to the high-speed nature of the gas flows employed (Carroll and Hidrovo 2013; Carroll and Hidrovo 2012a; b). These high inertial effects can also be leveraged to achieve microsecond processing times and tens of μL/min throughputs. Despite its significance and potential, the difficulties associated with proper gas–liquid flow control have limited the extent of experimental work conducted on these microfluidic devices. The majority of studies are therefore theoretical and numerical in nature (Gopinath and Koch 2001; Bach et al. 2004). Only a few experimental works are available in atmospheric phenomena, spray formation and combustion applications (Carroll and Hidrovo 2013; Marmottant and Villermaux 2004; Post and Abraham 2002). An understanding of high inertial droplet generation characteristics in gas–liquid systems at the microscale is essential to make gaseous digital droplet microfluidics systems a reality, achieving high throughputs and fast processing times that can lead to the development of next-generation Lab-on-a-Chip and micro-Total Analysis Systems. Similar to liquid–liquid droplet microfluidic applications, such as digital droplet PCR (dd-PCR) (Hindson et al. 2011), the large-scale discretization of the liquid phase on the gaseous environment could open the door for the digitization of these processes. In addition, the high-speed nature of these droplet flows can be exploited to enhance mixing through inertial droplet pair collisions (Carroll and Hidrovo 2012a; Carroll and Hidrovo 2012a). Note that, in addition to the pneumatic-based droplet generation, there have been extensive approaches to generate liquid droplets using active manipulations such as acoustic wave (Elrod et al. 1989), electrical signal (Gong and Kim 2008), heat (Tan et al. 2008a, b) and magnetic field (Zhang et al. 2009).

Although previous studies (Carroll and Hidrovo 2013; Gopinath and Koch 2001) have provided some insights about the dynamics of liquid droplet generation (discrete phase) in a gaseous flow (continuous phase), there are few studies that investigate the fundamental relationship between the discrete and continuous flow phases and the droplet generation regime and size.

In this paper, we demonstrate droplet formation in various flow-focusing geometries that produce high *Re* (~450) discrete gas–liquid flows in microfluidic devices. Different combinations of air and water flow rates create a map of flow regimes. The relationship between droplet diameters and gas flow rate was experimentally obtained in 60° flow-focusing geometry. Numerical simulations that predict this relationship have been performed and compared with the experimental results. The insight and possible applications of the high inertial droplet flows are also discussed.

2 Experimental

2.1 Experimental setup

The experimental setup, shown in Fig. 1a, enables time-resolved bright-field microscopy using a high-speed camera (up to 1.3 million frames/s) controlled by a customized

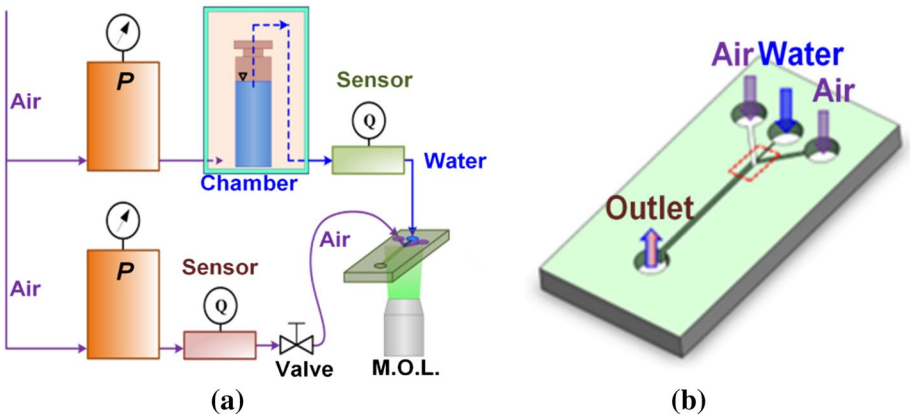

Fig. 1 Schematic of experimental setup and channel configuration. **a** Experimental setup includes pressure transducers (*P*), flow meters (*Q*), microscope objective lens (M.O.L), needle valve and pressurized chamber and **b** channel configuration in the PDMS microfluidic chip. The PDMS microchannels are molded by soft lithography techniques and include two inlets for air flow: one inlet for water flow and one outlet for two-phase flow

LabVIEW program. Precise droplet generation was controlled by regulating the upstream pressure of the gas and liquid inlet lines separately (Fig. 1a). For the gas stream, the air flow rate was controlled by a pressure regulator (Proportion Air) and a needle valve (Swagelok) positioned upstream of the microfluidic chip. The resolution of the pressure control with LabVIEW was 0.02 psi, and the maximum line pressure in all experiments was 16 psi. A volumetric flow meter (Sierra Instruments) installed before the needle valve monitored the air flow rate (Q_a). This single line of air flow was split into two separate flows right after the flow meter by a high-pressure fitting connected to the two air inlet ports in the microfluidic chip. Another pressure-regulated airline was connected into a custom aluminum chamber containing the water reservoir. Gradual pressurization of the chamber was used to control the water flow with values as low as 0.2 μL through a 1/16 inch tubing into the water inlet port in the chip. The water flow rate (Q_w) was measured by a liquid flow meter (Sensirion) just before the inlet port of the chip. An inverted microscope (Nikon) was used to image liquid droplets forming at the intersection of the gas–liquid outlets illuminated by a bright-field light source (Prior Scientific) through a 10× magnification microscope objective. A CMOS high-speed camera (Photron Fastcam SA5) was employed to collect sequential droplet images at the rate of 7000 frames per second.

2.2 Microfluidic chips

Microfluidic chips used in this study were fabricated by soft lithography with PDMS (polydimethylsiloxane). Most microfluidic devices composed of PDMS and glass are commonly assembled by a plasma treatment. Despite plasma-treated PDMS surfaces becoming hydrophilic, which leads to water droplets wetting and attachment to the microchannel walls, they can be made hydrophobic by treating them with hydrophobic or fluorophilic chemicals (Tan et al. 2010). More importantly, though, plasma-treated chips have a relatively weak bonding strength (Eddings et al. 2008) not capable of handling the pressures required for operation of the device. Although a previous study showed that plasma-bonded PDMS chips can withstand pressures as high as 30 psi (Thiele et al. 2011), we observed rupture of our particular design at the higher end of the pressures (16 psi) used in this study. For these reasons, we did not use plasma-treated chips for water droplet generation. Instead, we employed PDMS–PDMS bonding for both top and bottom pieces in this study. Si wafers containing the channel configurations were fabricated by standard photolithography using a negative SU-8 photoresist (Microchem 2075). PDMS microchannels were then molded by soft lithography involving four main steps. First, the PDMS mixture, which served as the top, main section piece, was prepared by mixing a silicon elastomer base and a curing agent at a 5:1 ratio. Then, the mixture was cured at 65 °C for 75 min on a hot plate. Second, a separate mixture of the elastomer base and the curing agent was mixed at a 10:1 ratio and served as the bottom piece. This 10:1 mixture was spin-coated on the glass slide using a customized fan at 500 rpm with a maximum thickness of 0.32 mm. The different mixing ratios between the top and bottom pieces promote diffusion of the cross-linkers, resulting in a permanent bond that is 50 % stronger than most other PDMS-bonding techniques (Eddings et al. 2008). Third, after partially curing the bottom piece at 70 °C for 25 min, the two pieces were brought into a conformal contact applying uniform pressure. Fourth, the assembled piece was cured on the hot plate at 65 °C for 24 h for strong bonding. Using this method, we could sustain more than 16 psi in our microfluidic chips. It is worth mentioning here that in recent work performed by this group it was shown that the Young's modulus of 5:1 PDMS is 20 % higher than that of 10:1 PDMS (Kim et al. 2013). Since the top, main section piece of the sample is made of the 5:1 PDMS (intrinsically stiffer), but the 10:1 bottom piece is substantially thinner (0.32 mm thick) and attached to the glass, we surmise that there is minimal degree of channel asymmetry due to mechanical deformation, and therefore, no preferential

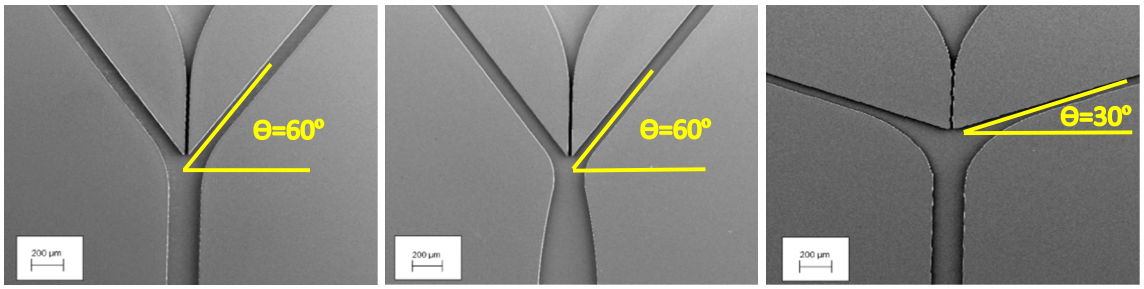

(a) (b) (c)

Fig. 2 Magnified view of the air–water junction showing detailed dimensional parameters. **a** 60° converging flow-focusing junction, **b** 60° converging–diverging flow-focusing junction and **c** 30° converging flow-focusing junction. Notice that the widths of the microchannels downstream of the flow-focusing junctions remain constant. 60° and 30° are complementary angles between air and water channels. All channels have a *rectangular* cross section (aspect ratio = 0.4–4) and are ~43 μm in depth. The widths of the inlet air and water channels are 100 and 20 μm, respectively. The main exit channel of the converging flow-focusing junction configuration is 200 μm in width, while the throat of the converging–diverging flow-focusing junction configuration is also 200 μm and the exit channel width is 400 μm

Table 1 Experimental contact angle measurements of original and fluorosilane-treated PDMS surfaces

	Original PDMS		Fluorosilane-treated PDMS	
Mixing ratio	10:1	5:1	10:1	5:1
Contact angle	111.6	113.3	113	118

wetting of these surfaces is observed. Similarly, the permeability of PDMS in air is known to be 3.6×10^{-2} μm^2/Pa s at 35 °C (Suh et al. 2004). The highest operation pressure in this study was 16 psi. At this pressure, the penetration depth of the air into the outer surfaces from the air channel is estimated to be around 20 μm. Although the room temperature was slightly lower than 35 °C, taking into consideration that there is little dependence of the permeability on temperature and 5 mm of PDMS thickness, the amount of air leakage due to permeation into the PDMS material is negligible at the pressure conditions tested. Our experimental assessment of air flow leakage also indicated that overall air leakage rate associated with the PDMS chips is around 1–2 %, within the accuracy of the flow meters employed, and therefore negligible for all effects and purposes. Figure 2 shows SEM images of representative 60° and 30° flow-focusing geometry microchannels.

2.3 Hydrophobicity of PDMS surfaces

Hydrophobicity of PDMS surfaces plays an important role in successful generation of water droplets in confided microchannels. Although the intrinsic contact angle of cured PDMS is known to be 105° (Haubert et al. 2006) which is hydrophobic, due to the contact angle hysteresis of water on the PDMS surfaces, water droplets and streams tend to stick to the wall and leave liquid residue and satellite droplets behind. Therefore, we further treated the cured PDMS surfaces of the microchannels with various techniques aimed at further increasing the hydrophobicity and reducing the hysteresis, including using very soft sandpaper (grit number 240) during the microfabrication process (mild sanding of the silicon SU-8 molds and coated glass slides) to enhance roughness (average surface roughness of 15 μm), post-thermal treatment of cured PDMS, Aquapel treatment of cured PDMS surfaces and fluorosilane deposition into the cured surfaces. Among them, we found that fluorosilane treatment was the most efficient technique to increase the hydrophobicity of the PDMS surfaces. In detail, one of the outlets of the cured PDMS chip was connected to one side of a peristaltic pump (Parker Corp.) through a 1/16 inch tubing, while the other side of the pump remains opened. A 50 μL fluorosilane was dropped on a glass slide next to the chip. The assembly of the chip–pump–glass slide was placed inside a vacuum chamber. Starting with the vacuum pump, the peristaltic pump was also powered to circulate fluorosilane molecules evaporated inside the chamber. After 2 h—which we found to be the optimal time for deposition—the fluorosilane-coated PDMS chip was taken out from the vacuum chamber and used for experiments. Experimental contact angle measurement of original and fluorosilane-treated PDMS surfaces is summarized in Table 1.

3 Results and discussion

3.1 Flow regime mapping

Three (3) types of PDMS chips with different flow-focusing geometries were tested: (a) 60° converging flow-focusing junction, (b) 60° converging–diverging flow-focusing junction and (c) 30° converging flow-focusing junction. The

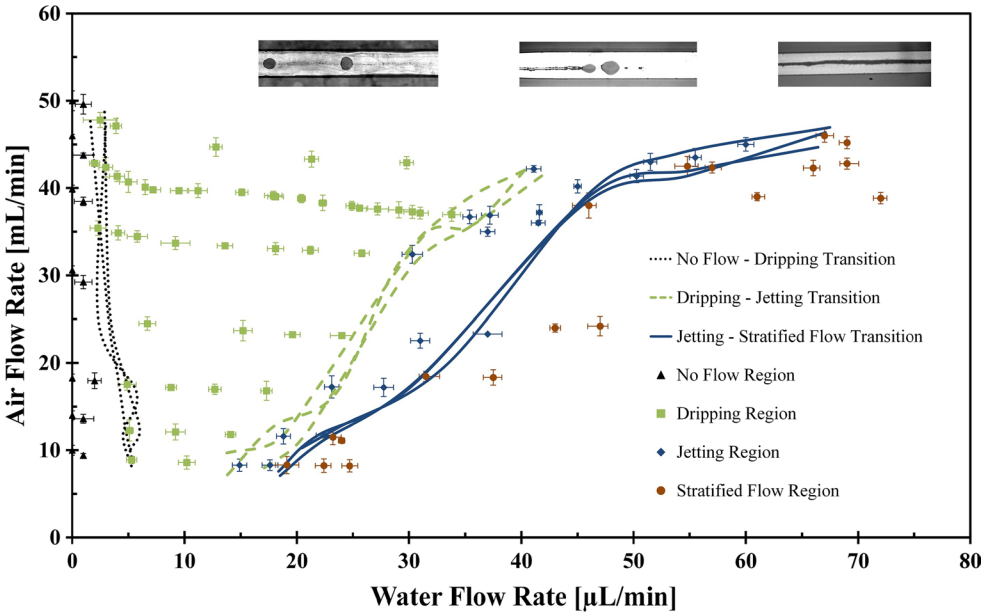

Fig. 3 Flow regime map for 60° converging configuration. Four different regimes were observed: No Flow region characterized by no droplet flow, Dripping region defined as droplet flows at certain frequencies pinched off at the junction, Jetting region described as droplet flows formed at the end of a thin liquid thread grown from the junction, and Stratified region specified as a stable co-flow of gas and liquid

rationale behind the choice of these designs was to explore (1) the effect that flow-focusing angle had on droplet formation, given that the air flow is a primary factor in the detachment process, and (2) the effect that a converging–diverging geometry, akin to "soft necking" section for liquid–liquid systems, would have on the process. The PDMS chips with different flow-focusing configurations described above were used to map the various flow regimes and transitions of the air–water flows. The flow regimes found were generally divided into three categories: Dripping (droplet formation at the junction), Jetting (liquid thread with tip streaming droplet generation) and Stratified Flow (stable co-flowing liquid and gas streams). The maps are plotted in terms of flow rates as per traditional convention when dealing with multiphase flows.

The flow regime mapping procedure consisted of setting a starting air flow rate (Q_a) while changing water flow rate (Q_w) in increments of 2–5 µL/min. As Q_w changes, the flow regimes were recorded and identified. The same procedure was carried out for various starting values of Q_a. Collecting data points in the reverse direction (setting Q_w first and then changing Q_a) was not possible since the microchannels would get flooded/filled with water and the air flow would not be able to overcome and remove it completely to establish a droplet-generating regime. So only a stratified regime is possible with this type of operation. Figure 3 shows the different flow regimes in the converging flow-focusing configuration with junction angle of 60°. At a given starting Q_a, as Q_w increases, three different flow regimes were identified: Dripping, Jetting and Stratified Flow. Each data point represents the average of three (3) experimental runs, and all the transition lines for each experiment have been included in this figure to provide a sense of the transition region uncertainty. No droplet flow or the No Flow regime is observed until Q_w reaches a certain threshold, which is the transition point to start the Dripping regime (Video 1 in supplementary information). The transition values of Q_w decrease as Q_a increases because the higher inertial air flow imposes a larger dynamic force to pinch-off the water droplets forming at the junction. By further increasing Q_w, beyond the transition, consistent droplet formation was observed. At a larger Q_w value, a thin liquid thread grows from the junction and the Dripping regime transitions to Jetting; however, droplets are formed at end of the thread (Video 2 in supplementary information). As Q_w is further increased, the tip of the stream keeps moving forward until it reaches the outlet port. Once the stream tip meets the outlet and a stable co-flow of gas and liquid streams is established, the flow is considered fully Stratified. The initial thickness of the stream depends on the ratio $Q^* = Q_w/Q_a$. Our observations revealed that by increasing Q^*, the thickness increases until the liquid flow fills the entire outlet channel. Multiple tests were performed for different microchannel samples for the same junction angle for repeatability. Although the air supply pressure is set to a constant value, Q_a changes from its initial value as Q_w is increased. As first, Q_a decreases in the No Flow and Dripping regime regions as the water and droplets present a large obstruction to the air flow. Once a liquid stream is formed in the Jetting and Stratified regime regions, the water obstruction is reduced and the air flow rates increase once again. These phenomena can be addressed and quantified by doing an order of magnitude calculation of the flow resistance changes under the presence of water droplets and streams. The hydrodynamic resistance of the flow channel is defined as $R_h = \Delta P/Q$ where ΔP is the applied pressure

drop through the channel and Q is the flow rate. For a rectangular channel, the flow resistance can be approximated as $R_h = 12\ \mu La/h^4\ (1 - 0.63a)$, where μ is the dynamic viscosity of the fluid, L is the channel length, and a is the ratio of channel height to channel width (h/w) (Tanyeri et al. 2011). From this equation, it is apparent that the flow resistance is very sensitive to h and w when the fluid and channel length remain constant. Tanyeri et al. showed that the flow resistance increases significantly when there exists a channel constriction within the outlet channel. Therefore, when the water flow rates increase and a larger number of droplets are present in the channel, the effective height and width for the air flow will be significantly decreased, resulting in a large increase in the flow resistance for the air flow. This explains the decrease in air flow rate as the water flow rate increases even if the input pressure of the air flow remains constant. An order of magnitude comparison between the No Flow region and Dripping region shows a 24 % increase in hydraulic resistance with average droplet size of 150 μm and five droplets present in the microchannel at any given time. Experimental results suggest a 20 % increase, which agrees with our order of magnitude analysis. The increase in hydraulic resistance for the Stratified Flow region is 13 % based on the order of magnitude analysis and 14.5 % experimentally, again showing good agreement between the basic theory and data.

In addition, dimensionless numbers for the liquid phase have been investigated in the flow regime map. Table 2 shows capillary number ($Ca_w = \mu_w V_w/\sigma_w$) and Weber number ($We_w = \rho_w V_w^2 D_{eff}/\sigma_w$) for the water flow at transition boundaries distinguished by air flow Reynolds number ($Re_a = \rho_a V_a D_{eff}/\mu_a$).

Although several factors affect the droplet detachment process, it is primarily related to the air flow conditions and occurs due to a balance between (1) the net air momentum flux (air inertial force), (2) the viscous pressure drop arising from the flow of air through the constriction created by the droplet and the channel, (3) the pressure difference between the liquid and air streams and (4) the surface tension of the droplet (see Sect. 3.2). On the other hand, transition from the Dripping regime into the liquid film displaying regimes (Jetting/Stratified) occurs when liquid inertia overcomes surface tension forces, disrupting the liquid containment effect provided by the droplet surface tension and leading to the formation of the film. This is evidenced in Table 2 where it can be seen that transition into liquid film displaying regimes occurs when $We \sim 0.1$–1, indicating that the inertia of the liquid flow is large enough to overcome the droplet surface tension forces at the junction location. It is also evident that the larger the gas flow Re number, the larger the liquid flow We number required for these transitions is. This can be explained by the fact that the larger gas flow rates, associated with larger Re numbers, lead to larger viscous pressure drops along the length of the droplets, which is the dominating force in detaching them from the injection point. The smaller the droplets formed at the injection point are, the larger the liquid inertia needed to "break up or disrupt the droplet" and transition the liquid flow from a droplet to a film regime, as dictated by the We number. Thus, at higher air flow rates, larger water flow rates are required to overcome the surface tension forces at the injection point and to lead the system to exhibit a Jetting regime.

Table 2 Capillary and Weber dimensionless numbers for air and liquid phases at transition boundaries

	Transition to Jetting		Transition to Stratified Flow	
	$Re_a \sim 75$	$Re_a \sim 380$	$Re_a \sim 75$	$Re_a \sim 420$
Ca_w number	3.86×10^{-3}	1.16×10^{-2}	5.15×10^{-3}	1.79×10^{-2}
We_w number	1.66×10^{-1}	1.49	2.94×10^{-1}	3.57

Figure 4 compares flow regime maps for junction angles of 30°and 60°. Rather than including all the different transitions lines for the different experiments as done in Fig. 3, only the "mean" transition line is presented with a thickness representative of the region uncertainty for the given transition. Similarly, the mean data points from 3 different experiments are being presented but without the error bars as in Fig. 3 for clarity of comparison between the two different geometries trends. It is apparent that the general patterns of the map for the 30° configuration are similar to those of the 60°. However, the flow regime transitions of the 30° configuration are shifted to the right, i.e., the transitions between No Flow–Dripping, Dripping–Jetting and Jetting–Stratified Flow start at the higher Q_w compared to those at 60°. Specifically, along the No Flow–Dripping transition line, a higher Q_w is required to form the droplets at the same Q_a. Air momentum flux perpendicular to the liquid flow (lateral inertial force) prevents lateral growth of the droplet or pinches the liquid stream, depending on which regime the flow is in. At smaller junction angles, this lateral component of air momentum flux increases, and therefore, a higher water flow rate is required to overcome surface tension and form a droplet. Same reasoning is valid for pinching the liquid stream at the Jetting–Stratified Flow transition.

Geometrical parameters play a major role in the droplet formation and detachment processes. Hence, optimization of droplet growth and pinch-off mechanics can be achieved through manipulation of the geometry and configuration at the injection section. In addition to varying the injection angles of the feeding channels, we also experimented with the introduction of a converging–diverging section at the injection junction that joins with the main channel section.

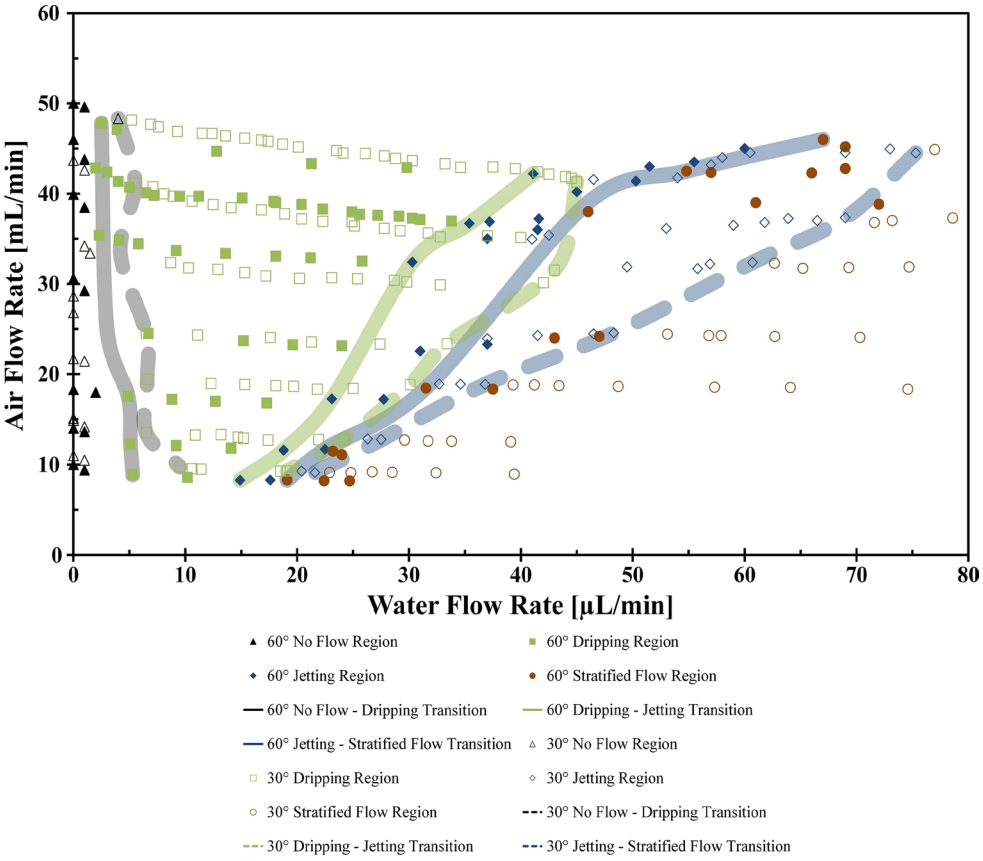

Fig. 4 Comparison of flow regime maps at 60° and 30° converging configurations. At 30° junction angle, a higher liquid flow rate is required to generate droplets since the gas momentum, which prevents lateral growth of droplet, increases. The same interpretation can be applied to the Dripping–Jetting transition

This section allows for a smoother transition of the gas flow over the droplet and also increases the pressure difference that contributes to droplet detachment. Although the air slow downs in the diverging portion of the converging–diverging geometry, detached droplets move out of the formation zone (throat section) before the next one is generated. In other words, droplets are being advected downstream faster than they are being generated. Figure 5 compares the flow regimes maps for a converging–diverging section with that of a converging section for 60° injection configuration. As depicted in the map, the converging–diverging configuration provides a wider region for droplet generation, especially in the Jetting regime. It also provides much larger throughputs in the Jetting regime compared to the converging configuration. Using the converging–diverging geometry essentially provides a pressure gradient in the channel, which is believed to facilitate detachment mechanism of droplets, separating them from the stream. In the normal geometry, the flow is forced to become a stream after a threshold value, which depends on various parameters (as obtained and shown in graphs); however, using the converging–diverging geometry, the threshold value is extended farther, due to the introduction of the pressure gradient. The pressure gradient enables the flow to reach higher flow rate and at the same time provides the condition in which droplets could be formed and detached.

If the water flow rate is large enough, it overcomes the viscous pressure drop responsible for the droplet formation and transitions the flow into the Stratified regime. In the converging–diverging geometry, the viscous pressure drop is higher, and therefore, a larger water flow rate is required for the transition to happen. This will result in a larger Jetting region. The same reasoning is valid for the Dripping region.

Before finishing this section, it is important to make a note regarding the nomenclature used for the film-bearing droplet-generating regime, namely the Jetting regime. The experimental and supporting video documentation presented here strongly suggest that this flow patterns is more akin to a rivulet (i.e., a small stream attached to the upper and lower channels walls) that emits droplets rather than a true jet. However, since we are not certain of this and trying to stay in line with the nomenclature used for liquid–liquid systems, we have employed the term Jetting. It is also important to note that if indeed the Jetting regime is a rivulet, pneumatic control of droplet generation in this regime might not be as effective given the interactions with the walls of both the film and the droplet themselves.

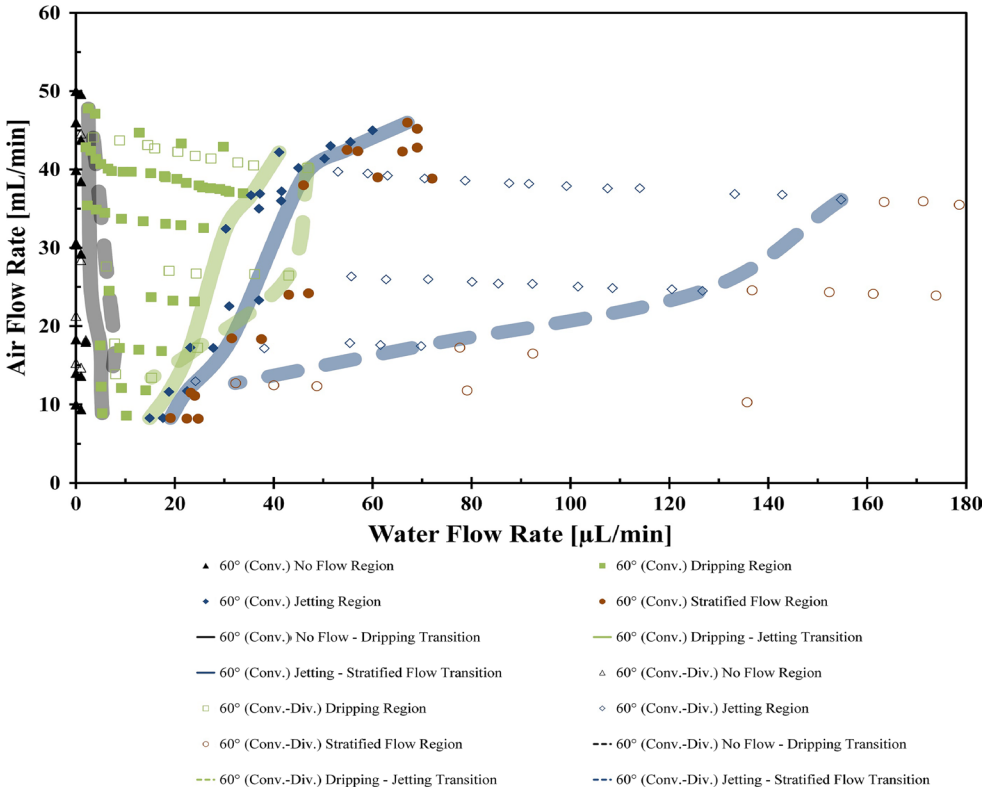

Fig. 5 Comparison of flow regime maps at 60° converging and converging–diverging configurations. The converging–diverging configuration provides a wider region for droplet generation and much larger throughputs in the Jetting regime compared to the converging configuration

As such, gas flow control is more effective in the Dripping regime.

3.2 Analytical modeling of droplet size and flow rate correlation

Understanding the governing physics behind droplet detachment is a vital step in designing optimal geometries for generating spherical liquid droplets in a gas environment at specific frequencies and sizes. In addition to flow regime mapping, we investigated the correlation of flow rate and droplet size under different flow conditions. In this section, we introduce analytical investigations of droplet detachment mechanism and compare these analyses with experimental results.

In conventional oil–liquid systems, it has been known that the interactions of inertia, shear stress, viscous and surface tension forces create unique liquid droplets in T-junction (Garstecki et al. 2006) or flow-focusing geometries (Christopher and Anna 2007). A recent study has summarized and compared the main observations and physical understanding of Dripping and Jetting regimes in different microfluidics geometries (Nunes et al. 2013). In order to analyze the forces acting on the liquid droplet in a gas environment, two control volumes were defined, as shown in Fig. 6. In Fig. 6a, we considered the control volume (A) stationary everywhere except at surface A_3, where the front is expanding at the droplet growing velocity. Then, the general form of the momentum equation was used to find the net force acting in x-direction. Three inertial terms were considered, including momentum flux of water and air entering the C.V. at A_1 and A_2, and air momentum exiting the C.V. at surface A_3. Due to the water/PDMS interfaces at the water inlet channel as well as the top and bottom surfaces, surface tension forces were accounted accordingly. A forward pressure force due to the pressure difference between the upstream and downstream sides of the control volume was also considered.

The same procedures were repeated for the control volume (B) in Fig. 6b to determine the lateral growth of the liquid droplet in the y-direction. The control volume (B) extends from the lower wall to just inside the droplet. The corresponding inertial terms and the pressure difference forces between the downstream and upstream locations were considered accordingly. In addition, the pressure force acting on the droplet in the y-direction due to the pressure difference between the inside and outside of the droplet should be accounted for. To find this force, the pressure difference between the inside and outside was assessed based on the mean droplet curvature and the Young–Laplace equation. The mean curvature can be measured by averaging the two principal curvatures of the droplet, namely the elliptical curvature in x–y plane and also the droplet curvature due to the hydrophobicity of PDMS to water in z–x plane using the results reported in Table 1. Then, by plugging the obtained

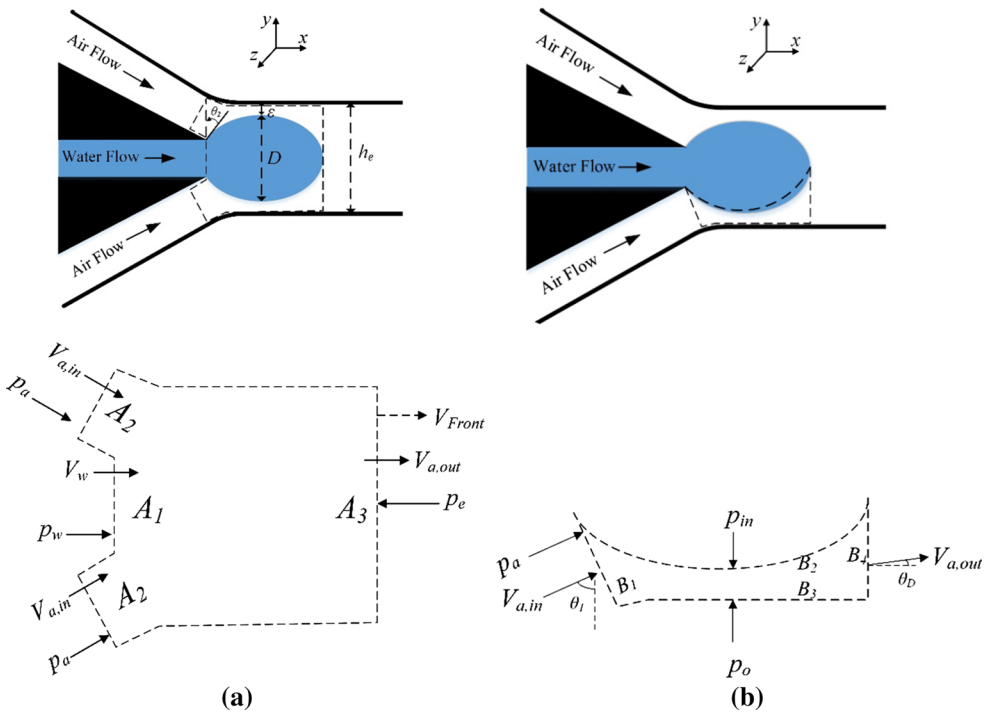

Fig. 6 Control volumes for the momentum analysis in **a** *x*-direction and **b** *y*-direction

Table 3 Symbol nomenclatures used in Eqs. (1) and (2)

Symbol	Description	Symbol	Description
Q_a	Flow rate of air in inlet channel	w	Depth of the system (in z-direction)
ρ_a	Density of air	P_w	Water pressure at inlet channel
μ_a	Viscosity of air	ε	Distance between droplet and sidewalls of the channel
Po	Poiseuille number	L_{ch}	Characteristic length of the droplet
D	Lateral dimension of droplet	h_a, h_w, h_e	Width of air inlet channel, water inlet channel and exit channel
$V_{a,in}$	Air velocity at air inlet channel	σ	Surface tension of water in air
P_a	Air pressure at air inlet channel	R_{hp}	Curvature radius due to hydrophobicity
θ_1	Shown in Fig. 6b	θ_2	Shown in Fig. 6a
A_i ($i = 1{:}4$)	Surfaces of control volume as shown in Fig. 6a	B_j ($j = 1{:}4$)	Surfaces of control volume as shown in Fig. 6b

mean curvature in the Young–Laplace equation, the corresponding pressure force was calculated.

In order to make this analytical problem mathematically traceable, we assumed that: (1) The droplet is perfectly elliptical in x–y plane. (2) Velocity of the air exiting the control volume (Fig. 6a) is much higher than the growth rate of the droplet front. (3) The air flow within the gap between the droplet and channel is laminar and fully developed. (4) Due to the low Mach number (<0.3) of the air flow in the gap, this flow was considered to be incompressible. (5) Due to low capillary number of the system, shear forces were neglected in this analysis. By employing these assumptions, the general momentum conservation on the droplet CV can be stated as:

$$[\text{Net momentum flux out}] = \sum F = [\text{Pressure forces}] + [\text{Surface tension forces}]. \tag{1}$$

The momentum flux terms include both the air and water flows. The contribution of the water momentum flux, however, shall be neglected as the Weber number for water is as small as ~0.01. Thus, the governing equations finally become

$$\left[\frac{\rho_a Q_a^2}{h_a w}\left(\frac{h_a}{h_e} - 2\sin\theta_1\right)\right] = \sum F_x = \left[(p_w - p_a)h_w w + \left(\frac{\text{Po}\,\mu_a L_{ch} Q_a}{w\varepsilon^3}\right)h_e w\right] - [\sigma(2w\sin\theta_2 + h_w + D)], \tag{2}$$

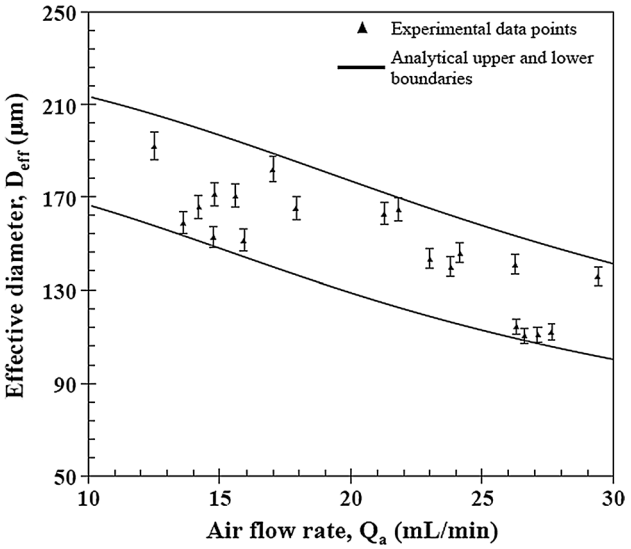

Fig. 7 Analytical and experimental results for droplet diameter versus air flow rate

$$\rho_a V_{a,in}^2 B_1 \cos\theta_1 = \sum F_y = \left[\sigma\left(\frac{2}{D} + \frac{1}{R_{hp}}\right)B_3 + P_a B_1 \cos\theta_1\right] - [\sigma D]. \quad (3)$$

Detailed description of the characters used in these equations is provided in Table 3.

As shown in Eqs. (1) and (2), net forces in both *x*-direction and *y*-direction are the summation of terms representing pressure forces and forces due to surface tension which must balance the net momentum flux out of the CV, which is given by the outlet and inlet flow conditions of the air. Based on our experimental observations, the diameter of the droplet continues to grow laterally until it stops at its maximum diameter and stays stationary. Since this lack of droplet growth represents a steady-state condition, we can conclude that the final diameter can be found using Eq. (3). Also, we experimentally observed that the growing rate of the droplet in *x*-direction is almost non-existent at the moment of detachment; therefore, we can also claim steady-state conditions and Eq. (2) equally applies.

In Eqs. (2) and (3), the lateral dimension of the droplet (D) and the characteristic length (L_{ch}) are the unknown parameters. Thus, at a given air flow rate and pressure difference ($P_w - P_a$), the final diameter of the droplet (D_{eff}) can be simply calculated. The Newton–Raphson method was then implemented in MATLAB to solve the system of equations, iteratively. We evaluated the system of equations within the pressure range in which Dripping was observed. To obtain the final diameter of the droplet, we assumed that the droplet forms a perfect spherical shape after the detachment. Thus, we defined the effective diameter as

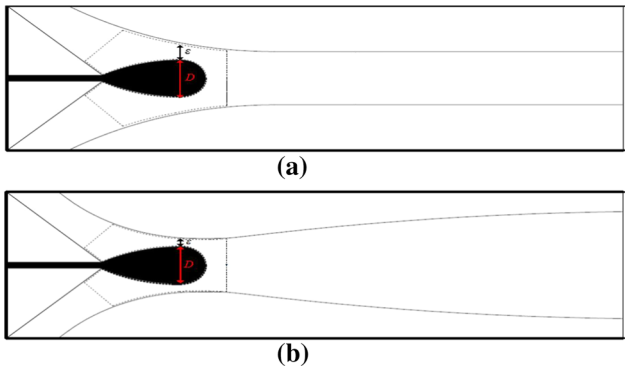

Fig. 8 **a** Converging channel and **b** converging–diverging channel. The converging–diverging geometry results in a much smaller gap between channels walls and the droplet, resulting in larger viscous pressure gradient and corresponding pressure drop along the length of the droplet, leading to a larger net droplet detachment force

$D_{eff} = \left(\frac{3}{2} \times D \times L_{ch} \times w\right)^{1/3}$ where D is the lateral dimension calculated earlier. Figure 7 shows experimental and analytical results of the effective droplet diameter as functions of air flow rate. In the experiments, effective droplet diameters decrease with increasing air flow rate. The higher air flow rates induce higher momentum flux changes and pressure differences across the droplets, leading to smaller effective droplet diameters. The upper and lower bounds for the expected effective droplet diameters in the numerical analysis can be found by solving Eqs. (1) and (2). These bounds are computed using the maximum and minimum pressure differences employed to generate the flow regime map. It must be noted that for a given nominal flow rate, different pressure differences could be in play because there could be multiple water input pressures that would correspond to the same air flow rate, due to the unstable nature of the two-phase flow.

As illustrated in Fig. 7, the analytical model bounds the experimental results well by fitting all the experimental data points within the predicted range. The implemented analytical model predicted the effective droplet diameter with the uncertainty of ~10 % at a given air flow rate. It should be noted that the droplet diameter has a weak dependence on Q_w as detachment is more directly related to air flow rate.

By taking a closer look at Eq. (2), it is apparent that the net detachment force is highly dependent on the geometrical dimensions of the detachment section. Hence, adjustment of these dimensions has a significant effect on the droplet formation and growth. As illustrated in Fig. 8, in a converging–diverging channel, the location of minimum width is closer to the droplet generation zone (in our design the 200 μm width), and this will result in a smaller gap

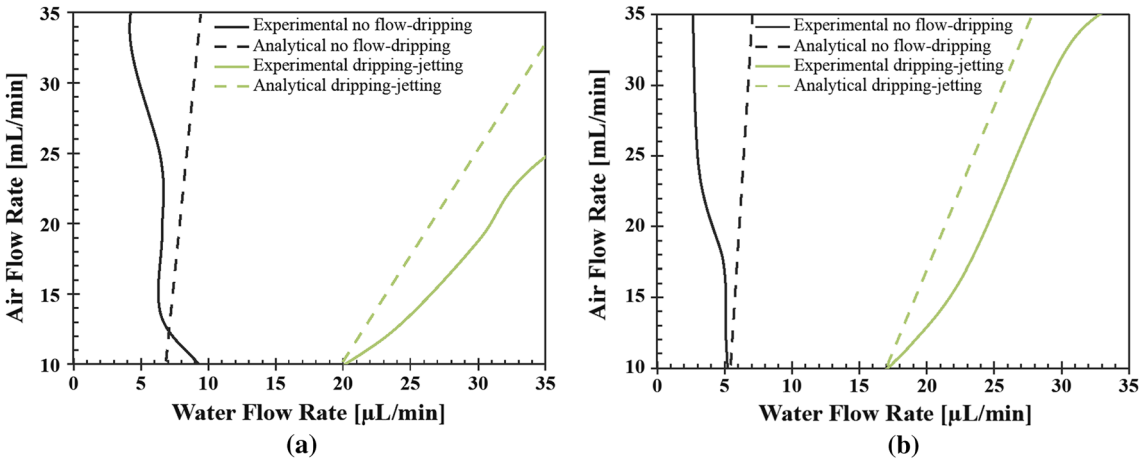

Fig. 9 Comparison of experimental and analytical transition lines of No Flow–Dripping and Dripping–Jetting for two different geometries of **a** 30° and **b** 60°

between droplet and walls [smaller ε in Eq. (2)]. Hence, the air flow is squeezed through a narrower path resulting in a larger viscous pressure gradient and corresponding pressure drop along the length of the droplet, leading to a larger net droplet detachment force.

The droplet detachment analysis can be further used to better understand the transition trends of the system from the No Flow to Dripping regime and similarly from the Dripping to Jetting regime. From Eqs. (2) and (3), one can simply determine the effective diameter of the droplet at a given air flow rate. Moreover, as described earlier, the transition from No Flow to Dripping and also Dripping to Jetting occurs at a specific range of Capillary and Weber numbers. Thus, using the reported values for *We* number in Table 2, we can find the water flow rate in which the regime of the flow changes by using as characteristic length scale for *We* the droplet diameter for a given air flow rate. This provides a rough order of magnitude analysis in terms of the water flow rate inertia required to overcome surface tension forces and (1) create a droplet in the transition from No Flow to Dripping, and (2) shift from a droplet to a jet in the transition from Dripping to Jetting. In Fig. 9, the analytical transition lines are illustrated and compared to those of experimentally obtained, for two different geometries of 30° and 60° junction. As was observed experimentally, the water flow rate does not have a substantial effect on the droplet detachment. This effect is well captured in our analytical transition line for the case of No Flow–Dripping. However, at higher flow rates of air, shear stress between the air and the droplet becomes large enough to exert a considerable force in the direction of the water flow; therefore, lower values of water inertia are needed to form a droplet. Neglecting the effect of this force causes our model to overpredict the required water flow rate for the No Flow–Dripping regime transition, especially at higher air flow rates. On the other hand, the transition from Dripping to Jetting occurs at higher values of water flow rate than our transition analysis would predict. This is the result of neglecting the water momentum flux (water flow inertia) in our droplet detachment forces model (Eq. 2), which leads to overprediction of the droplet detachment diameter at larger water flow rates. A larger droplet detachment diameter corresponds to a lower water flow rate needed for transition, as postulated by the *We* number. Hence, our Dripping–Jetting transition analysis under-predicts the water flow rate needed for this transition to happen, and as such, this discrepancy with the experimental results grows as the water flow rate increases.

4 Conclusions

Controlled and repeatable gas–liquid droplet generation and transport through pneumatic actuation present many possibilities for microfluidic applications requiring the presence of a gaseous phase, such as detection of airborne particles. Similar to liquid–liquid droplet microfluidic applications, such as digital droplet PCR (dd-PCR), the large-scale discretization of the liquid phase on the gaseous environment could open the door for the digitization of these processes. In addition, the high-speed nature of these droplet flows can be exploited to enhance mixing through inertial droplet pair collisions.

In this study, we mapped different flow regimes for gas–liquid droplet generation under highly inertial conditions ($Re \sim 450$) for different flow-focusing configurations. The flow regimes found were divided into three categories: Dripping (droplet formation at the junction), Jetting (liquid

thread with tip streaming droplet generation) and Stratified Flow (stable co-flowing liquid and gas streams). We also observed that configurations with a higher junction angles initiate stable droplet generation sooner than those with lower angles. In addition, the converging–diverging junction configuration is also beneficial in terms of providing a larger map space for stable droplet generation. It encourages clean detachment of the droplets and ensures for a smoother transition into the main microchannel section. A larger water flow rate (Q_w) is required to achieve the same type of flow with the converging–diverging configurations than with converging channels. In converging–diverging geometries, Q_w in the Dripping regime ranged from 2 to 50 μL/min with accompanying Q_a ranging from 8 to 50 mL/min (Fig. 4). In summary, we observed that a converging–diverging geometry at a high junction angle is the most favorable in terms of generating stable droplets and larger operating regions for both Dripping and Jetting. In addition to flow regime mapping, an analytic approach was taken to better understand governing physics underlying detachment process. We analyzed the correlation of flow rate and droplet size under different flow conditions.

It is important to note here that although a holistic approach to the practical implementation of gas-based droplet microfluidic systems in LOC applications would also involve droplet manipulation and collection, the focus of this paper and work has been on the specific task of droplet generation. As such, the droplets generated in the devices used in this study simple coalesce and merge at the exit of the device. Our group is currently working on the tasks of droplet collection and manipulation after generation in these gaseous systems.

The contributions presented in this paper provide new insights into the emerging field of high-speed gas–liquid droplet microfluidics. It sets the foundations for further studies in this field, which can lead to the development of next-generation droplet microfluidic devices for gas–liquid applications that can benefit from digitization of its associated biochemical processes.

Acknowledgments This work was supported by DARPA 2008 Young Faculty Award (YFA) grant HR0011-08-1-0045 and is currently being supported by an NSF CAREER Award grant CBET-1151091. Authors thank Dr. Brian Carroll and David Choi for their helpful discussions for the experimental setup and Kevin Choi for his assistance in fabrication of microfluidic chips.

References

Ahn CH, Choi J, Beaucage G, Nevin JH, Lee J, Puntambekar A, Lee JY (2004) Disposable smart lab on a chip for point-of-care clinical diagnostics. IEEE 92:154–173

Anna SL, Bontoux N, Stone HA (2003) Formation of dispersions using flow focusing in microchannels. Appl Phys Lett 82:364–366

Aryafar H, Kavehpour HP (2006) Droplet coalescence through planar surfaces. Phys Fluids 18:072105

Atencia J, Beebe J (2004) Controlled microfluidic interfaces. Nature 437:648–655

Bach GA, Koch DL, Gopinath A (2004) Coalenscence and bouncing of small aerosol droplets. J Fluid Mech 518:157–185

Bedram A, Moosavi A (2011) Droplet breakup in an asymmetric microfluidic T Junction. Eur Phys J E Soft Matter 34:1–8

Ben-Tzvi P, Rone W (2010) Microdroplet generation in gaseous and liquid environments. Microsyst Technol 16:333–356

Bolognesi G, Hargreaves A, Ward AD, Kirby AK, Bain CD, Ces O (2015) Microfluidic generation of monodisperse ultra-low interfacial tension oil droplets in water. RSC Adv 5:8114–8121

Buie CR, Santiago JG (2009) Two-phase hydrodynamics in a miniature direct methanol fuel cell. Int J Heat Mass Transf 52:5158–5166

Carroll B, Hidrovo CH (2012a) Droplet collision mixing diagnostics using single fluorophore LIF. Exp Fluids 53:1301–1316

Carroll B, Hidrovo CH (2012b) Experimental investigation of inertial mixing in colliding droplets. Heat Transf Eng 34:1–12

Carroll B, Hidrovo CH (2013) Droplet detachment mechanism in a high-speed gaseous microflow. J Fluid Eng 135:071206

Chen YT, Chang WC, Fang WF, Ting SC, Yao DJ, Yang JT (2012) Fission and fusion of droplets in a 3-D crossing microstructure. Microfluid Nanofluid 13:239–247

Choi S, Park JK (2005) Microfluidic system for dielectrophoretic separation based on a trapezoidal electrode array. Lab Chip 5:1161–1167

Chong ZZ, Tor SB, Loh NH, Wong TN, Gñáan-Calvo AM, Tan SH, Nguyen NT (2015) Acoustofluidic control of bubble size in microfluidic flow-focusing configuration. Lab Chip 15:996–999

Christopher GF, Anna SL (2007) Microfluidic methods for generating continuous droplet streams. J Phys D Appl Phys 40:R319–R336

Dolovich MB, Dhand R (2011) Aerosol drug delivery: developments in device design and clinical use. Lancet 377:1032–1045

Eddings MA, Johnson MA, Gale BK (2008) Determining the optimal PDMS-PDMS bonding technique for microfluidic devices. J Micromech Microeng 18:067001

Elrod SA, Hadimioglu B, Khuri-Yakub BT, Rawson EG, Richley E, Quate CF, Mansour NN, Lundgren TS (1989) Nozzleless droplet formation with focused acoustic beams. J Appl Phys 65:3441–3447

Fair RB (2007) Digital microfluidics: is a true lab-on-a-chip possible? Microfluid Nanofluid 3:245–281

Garstecki P, Gitlin I, DiLuizio W, Whitesides GM, Kumacheva E, Stone HA (2004) Formation of monodisperse bubbles in a microfluidic flow focusing device. Appl Phys Lett 85:2649–2651

Garstecki P, Fuerstman MJ, Stone HA, Whitesides GM (2006) Formation of droplets and bubbles in T-junction—scaling and mechanism of breakup. Lab Chip 6:437–446

Gong J, Kim CJ (2008) All-electronic droplet generation on-chip with real-time feedback control for EWOD digital microfluidics. Lab Chip 8:898–906

Gong X, Miller PW, Gee AD, Long NJ, de Mello AJ, Vilar R (2012) Gas–liquid segmented flow microfluidics for screening Pd-Catalyzed carbonylation reactions. Chem Eur J 18:2768–2772

Gopinath A, Koch DL (2001) Dynamics of droplet rebound from a weakly deformable gas–liquid interface. Phys Fluid 13:3526–3532

Haubert K, Dryer T, Beebe D (2006) PDMS bonding by means of a portable, low-cost corona system. Lab Chip 6:1548–1549

Hayward RC, Utada AS, Dan N, Weitz DA (2006) Dewetting instability during the formation of polymersomes from block-copolymer-stabilized double emulsions. Langmuir 22:4457–4461

Hindson BJ, Ness KD, Masquelier DA, Belgrader P, Heredia NJ, Makarewicz AJ, Bright IJ, Lucero MY, Hidessen AL, Legler

TC, Kitano TK, Hodel MR, Petersen JF, Wyatt PW, Steenblock ER, Shah PH, Bousse KJ, Troup CB, Mellen JC, Wittmann DK, Erndt NG, Cauley TH, Koehler RT, So AP, Dube S, Rose KA, Montesclaros L, Wang S, Stumbo DP, Hodges SP, Romine S, Milanovich FP, White HE, Regan JF, Karlin-Neumann GA, Hindson CM, Saxonov S, Colston BW (2011) High-throughput droplet digital PCR system for absolute quantitation of DNA copy number. Anal Chem 83(22):8604–8610

Hu W, Ohta AT (2011) Aqueous droplet manipulation by optically induced Marangoni circulation. Microfluid Nanofluid 11:307–316

Jung JH, Lee KH, Lee KS, Ha BH, Oh YS, Sung HJ (2013) Optical separation of droplets on a microfluidic platform. Microfluid Nanofluid 16:635–644

Kim M, Moon BU, Hidrovo CH (2013) Enhancement of the thermomechanical properties of PDMS molds for the hot embossing of PMMA microfluidic devices. J Micromech Microeng 23:095024

Li W, Pham HH, Nie Z, Macdonald B, Guenther A, Kumacheva E (2008) Multi-step microfludic polymerization reactions conducted in droplets: the internal trigger approach. Am Chem Soc 130:9935–9941

Link DR, Grasland-Mongrain E, Duri A, Sarrazin F, Cheng ZD, Cristobal G, Marquez M, Weitz DA (2006) Electric control of droplets in microfluidic devices. Angew Chem Int Ed 45:2556–2560

Liu K, Ding H, Chen Y, Zhao XZ (2007) Droplet-based synthetic method using microflow focusing and droplet fusion. Microfluid Nanofluid 3:239–243

Lorenceau E, Utada AS, Link DR, Cristobal G, Joanicot M, Weitz DA (2005) Generations of polymerosomes from double-emulsions. Langmuir 21:9183–9186

Marine NA, Klein SA, Posner JD (2009) Partition coefficient measurements in picoliter drops using a segmented flow microfluidic device. Anal Chem 81:1471–1476

Marmottant P, Villermaux E (2004) On spray formation. J Fluid Mech 498:73–111

Mulligan MK, Rothstein JP (2012) Scale-up and control of droplet production in coupled microfluidic flow-focusing geometries. Microfluid Nanofluid 13(1):65–73

Nunes JK, Tsai SSH, Wan J, Stone HA (2013) Dripping and jetting in microfluidic multiphase flows applied to particle and fibre synthesis. J Phys D Appl Phys 46:114002

Piorek BD, Lee SJ, Santiago JG, Moskovits M, Banerjee S, Meinhart CD (2007) Free-surface microfluidic control of surface-enhanced Raman spectroscopy for the optimized detection of airborne molecules. PNAS 104:18898–18901

Post SL, Abraham J (2002) Modeling the outcome of drop–drop collisions in Diesel sprays. Int J Multiph Flow 28:997–1019

Priest C, Herminghaus S, Seemann R (2006) Generation of monodisperse gel emulsions in a microfluidic device. Appl Phys Lett 88:024106

Roberts CC, Rao RR, Loewenberg M, Brooks CF, Galambos P, Grillet AM, Nemer MB (2012) Comparison of monodisperse droplet generation in flow focusing devices with hydrophilic and hydrophobic surfaces. Lab Chip 12:1540–1547

Seemann R, Brinkmann M, Pfohl T, Herminghaus S (2012) Droplet based microfluidics. Rep Prog Phys 75:016601

Shabani R, Cho HJ (2013) Flow rate analysis of an EWOD-based device: how important are wetting-line pinning and velocity effects? Microfluid Nanofluid 15:587–597

Song H, Chen DL, Ismagilov RF (2006) Reactions in droplets in microfluidic channels. Angew Chem Int Ed 45:7336–7356

Song Y, Baudoin M, Manneville P, Baroud CN (2011) The air–liquid flow in a microfluidic airway tree. Med Eng Phys 33:849–856

Suh KY, Kim P, Lee HH (2004) Capillary kinetics of thin polymer films in permeable microcavities. Appl Phys Lett 85:4019–4021

Sun X, Tang K, Smith RD, Kelly RT (2013) Controlled dispensing and mixing of pico-to nanoliter volumes using on-demand droplet-based microfluidics. Microfluid Nanofluid 15:117–126

Tan YC, Cristini V, Lee AP (2006) Monodispersed microfluidic droplet generation by shear focusing microfluidic device. Sens Actuators B Chem 114:350–356

Tan SH, Murshed SMS, Nguyen NT, Wong TN, Yobas L (2008a) Thermally controlled droplet formation in flow focusing geometry: formation regimes and effect of nanoparticle suspension. J Phys D Appl Phys 41:165501

Tan YC, Ho YL, Lee AP (2008b) Microfluidic sorting of droplets by size. Microfluid Nanofluid 4:343–348

Tan SH, Nguyen NT, Chua YC, Kang TG (2010) Oxygen plasma treatment for reducing hydrophobicity of a sealed polydimethylsiloxane microchannel. Biomicrofluid 4:032204

Tanyeri M, Ranka M, Sittipolkul N, Schroeder CM (2011) A microfluidic-based hydrodynamic trap: design and implementation. Lab Chip 11:1786–1794

Thiele J, Windbergs M, Abate AR, Trebbin M, Shum HC, Forster S, Weitz DA (2011) Early development drug formulation on a chip: fabrication of nanoparticles using a microfluidic spray dryer. Lab Chip 11:2362–2368

Thorsen T, Roberts RW, Arnold FH, Quake SR (2001) Dynamic pattern formation in a vesicle-generating microfluidic device. Phys Rev Lett 86:4163–4166

Utada AS, Lorenceau E, Link DR, Kaplan PD, Stone HA, Weitz DA (2005) Monodisperse double emulsions generated from microcapillary device. Science 308:537–541

van Dijke K, Kobayashi I, Schroën Uemura K, Nakajima M, Boom R (2010) Effect of viscosities of dispersed and continuous phases in microchannel oil-in-water emulsification. Microfluid Nanofluid 9:77–85

Wada Y, Schmidt MA, Jensen KF (2006) Flow distribution and ozonolysis reaction in gas–liquid multichannel microreactors. Ind Eng Chem Res 45:8036–8042

Wan J, Stone HA (2012) Coated gas bubbles for the continuous synthesis of hollow inorganic particles. Langmuir 28:37–41

Wheeler AR, Moon H, Bird CA, Ogorzalek Loo RR, Kim CJ, Loo JA, Garrell RL (2005) Digital microfluidics with in-line sample purification for proteomics analyses with MALDI-MS. Anal Chem 77:534–540

Xu JH, Li SW, Tan J, Luo GS (2008) Correlations of droplet formation in T-junction microfluidic devices: from squeezing to dripping. Microfluid Nanofluid 5:711–717

Xu Q, Hashimoto M, Dang TT, Hoare T, Kohane DS, Whitesides GM, Langer R, Anderson DG (2009) Preparation of monodisperse biodegradable polymer microparticles using a microfluidic flow-focusing device for controlled drug delivery. Small 5:1575–1581

Yang SM, Yao H, Zhang D, Li WJ, Kung HF, Chen SC (2015) Droplet-based dielectrophoresis device for on-chip nanomedicine fabrication and improved gene delivery efficiency. Microfluid Nanofluid 19:235–243

Yasuda T, Imamura K, Hirase K (2009) Droplet transportation using EWOD-induced wettability gradient. In: Solid-state sensors, actuators and microsystems conference (Transducers), pp 413–416

Yobas L, Martens S, Ongand WL, Ranganathan N (2006) High-performance flow-focusing geometry for spontaneous generation of monodispersed droplets. Lab Chip 6:1073–1079

Zhang K, Liang Q, Ma S, Mu X, Hu P, Wang Y, Luo G (2009) On-chip manipulation of continuous picoliter-volume superparamagentic droplets using a magnetic force. Lab Chip 9:2992–2999

Zhou CF, Yue PT, Feng JJ (2006) Predicting sizes of droplets made by microfluidic flow-induced dripping. Phys Fluids 18:092105